Geophysical Journal International

*Geophys. J. Int.* (2014) doi: 10.1093/gji/ggt510

**Geophysical Journal International Advance Access published January 22, 2014**

# Statistical assessment of predictive modelling uncertainty: a geophysical case study

Riccardo Barzaghi,[1] Anna Maria Marotta,[2] Raffaele Splendore,[2] Carlo De Gaetani[1] and Alessandra Borghi[1]

[1] *DICA, Politecnico di Milano, Piazza Leonardo da Vinci* 32, *I*-20133 *Milan, Italy*
[2] *Section of Geophysics, Department of Earth Sciences 'A. Desio', Università degli Studi di Milano, L. Cicognara* 7, *I*-20129 *Milan, Italy.*
*E-mail: anna.maria.marotta@unimi.it*

Accepted 2013 December 17. Received 2013 October 31; in original form 2012 September 17

## SUMMARY

When the results of geophysical models are compared with data, the uncertainties of the model are typically disregarded. This paper proposes a method for defining the uncertainty of a geophysical model based on a numerical procedure that estimates the empirical auto- and cross-covariances of model-estimated quantities. These empirical values are then fitted by proper covariance functions and used to compute the covariance matrix associated with the model predictions. The method is tested using a geophysical, spherical, thin-sheet finite element model of the Mediterranean region. Using a $\chi^2$ analysis, the model's estimated horizontal velocities are compared with the velocities estimated from permanent GPS stations while taking into account the model uncertainty through its covariance structure and the covariance of the GPS estimates. The results indicate that including the estimated model covariance in the testing procedure leads to lower observed $\chi^2$ values and might help a sharper identification of the best-fitting geophysical models.

**Key words:** Numerical solutions; Numerical approximations and analysis.

## INTRODUCTION

Over the last several decades, analytical and numerical predictive models and the integrated interpretation of different types of natural data (geophysical, geodetic and geological) have played increasingly important roles in the interpretation of major crustal and mantle processes, such as subduction, continental collisions and intracontinental deformation. However, although comparisons between model predictions and data may be powerful in reducing the ambiguities between different geodynamic hypotheses, the absence of model uncertainty analysis limits this type of investigation. Consequently, the results of comparative analyses may be misleading, due to incomplete statistical analysis. To overcome this limitation, we devised a method accounting for model uncertainty through a model covariance structure. A methodology in which a model covariance matrix, $C_{\text{model}}$, associated to the model predicted velocities, is built that can be used with the covariance matrix from the observed data, $C_{\text{data}}$, associated to GPS-derived velocities, in a testing procedure. This methodology has been applied using a thin-sheet finite element geophysical model over the central Mediterranean area.

The advantage of this methodology is demonstrated by performing an analysis of model predictions and the corresponding observed data using a $\chi^2$ statistic in which the model and data covariance matrices are both taken into account.

## MODEL COVARIANCE MATRIX ESTIMATION

The method to account for model uncertainties has been devised for a particular geophysical model allowing the estimate of horizontal crustal velocities to be compared with GPS-derived velocities. However, this method can be used for any model (depending in a linear way from a set of parameters) when comparing model predictions and corresponding observed values.

The key point of the proposed method is the definition of the model covariance matrix. In our example, we use the spherical finite element model of Marotta & Sabadini (2004), as modified by Splendore *et al.* (2010), as a case study. This model predicts the horizontal surface velocities within a continental plate given defined velocity and thermal boundary conditions (see Appendix for details of the model). In particular, we assume the boundary conditions of their best-fitting model, which accounts for 50 per cent of the Africa–Eurasia convergence transmitted through the Calabrian subduction zone.

**Table 1.** List of the parameters responsible for the main variability of the model results.

| | Parameter | Value | References |
|---|---|---|---|
| Upper crust | Density $\rho$ (kg m$^{-3}$) | 2650 ÷ 2950 | Vilà *et al.* (2010) |
| | Radiogenic heat production $H$ (W m$^{-3}$) | $0.18 \times 10^{-6} \div 3.23 \times 10^{-6}$ | |
| | Conductivity $K$ (Wm$^{-1}$ K$^{-1}$) | 2.2 ÷ 3.9 | Roy *et al.* (1981), Drury (1986), Rybach (1988), Barker (1996), Artemieva & Mooney (2001), Beardsmore & Cull (2001), Jiménez-Munt *et al.* (2003), Ray *et al.* (2003), Afonso & Ranalli (2004), Vilà *et al.* (2010) |
| | Activation energy $E$ (J mol$^{-1}$) | $123 \times 10^3 \div 243 \times 10^3$ | Hansen & Carter (1982), Ranalli & Murphy (1987), Schaocheng *et al.* (2003), Afonso & Ranalli (2004) |
| | $n$ | 2.4 ÷ 3.9 | |
| | Pre-exponential factor $A$ (Pa$^{-n}$ s$^{-1}$) | $2.285 \times 10^{-30} \div 20.095 \times 10^{-22}$ | |
| Lower crust | Density $\rho$ (kg m$^{-3}$) | 2750 ÷ 2900 | Vilà *et al.* (2010) |
| | Radiogenic heat production $H$ (W m$^{-3}$) | $0.35 \times 10^{-6} \div 1.61 \times 10^{-6}$ | |
| | Conductivity $K$ (Wm$^{-1}$ K$^{-1}$) | 1.9 ÷ 2.5 | Roy *et al.* (1981), Drury (1986), Rybach (1988), Barker (1996), Artemieva & Mooney (2001), Beardsmore & Cull (2001), Jiménez-Munt *et al.* (2003), Ray *et al.* (2003), Afonso & Ranalli (2004), Vilà *et al.* (2010) |
| | Activation energy $E$ (J mol$^{-1}$) | $219 \times 10^3 \div 445 \times 10^3$ | Hansen & Carter (1982), Ranalli & Murphy (1987), Schaocheng *et al.* (2003), Afonso & Ranalli (2004) |
| | $n$ | 2.4 ÷ 4.2 | |
| | Pre-exponential factor $A$ (Pa$^{-n}$ s$^{-1}$) | $8.833 \times 10^{-22} \div 5.024 \times 10^{-18}$ | |
| Mantle | Density $\rho$ (kg m$^{-3}$) | 3200 ÷ 3300 | Vilà *et al.* (2010) |
| | Radiogenic heat production $H$ (W m$^{-3}$) | $0.002 \times 10^{-6} \div 0.03 \times 10^{-6}$ | |
| | Conductivity $K$ (Wm$^{-1}$ K$^{-1}$) | 3.0 ÷ 4.15 | Roy *et al.* (1981), Drury (1986), Rybach (1988), Barker (1996), Artemieva & Mooney (2001), Beardsmore & Cull (2001), Jiménez-Munt *et al.* (2003), Ray *et al.* (2003), Afonso & Ranalli (2004), Vilà *et al.* (2010) |
| | Activation energy $E$ (J mol$^{-1}$) | $260 \times 10^3 \div 532 \times 10^3$ | Chopra & Peterson (1981), Ranalli & Murphy (1987), Afonso & Ranalli (2004) |
| | $n$ | 3.0 ÷ 3.5 | |
| | Pre-exponential factor $A$ (Pa$^{-n}$ s$^{-1}$) | $2.5 \times 10^{-17} \div 4 \times 10^{-12}$ | |
| | Reference strain rate $\dot{\varepsilon}_0$ (s$^{-1}$) | $10^{-17} \div 10^{-15}$ | This work |
| Lithosphere | Reference thickness $h_L$ (km) | 80 ÷ 140 | This work |
| Velocity boundary conditions uncertainty | Modulus $\Delta U$ (cm yr$^{-1}$) | ±0.153 | This work: based on ITRF05 solutions (Altamimi *et al.* 2007) |
| | Azimuth $\Delta\phi$ (°) | ±0.784 | |

Table 1 lists the 22 parameters that have been identified as being responsible for the variability of the model results. The model considers a variety of layer compositions. Specifically, the upper crust is composed of granite, felsic granulite or quartzite; the lower crust is composed of diorite, mafic granulite or felsic granulite and the lithospheric mantle is composed of olivine, dunite or peridotite. We also assume that the thickness of the lithosphere varies between 80 and 140 km and that the reference strain rate varies between $10^{-17}$ and $10^{-15}$ s$^{-1}$. Finally, changes in the velocity boundary conditions along the southern boundary of the model are calculated by applying the classical error propagation procedure to the Eulerian pole procedure described in Splendore *et al.* (2010) and by calculating the Africa–Eurasia convergence.

Feasible minimum and maximum values for each model parameter are defined based on the literature. These values are assumed to compute the mean and the standard deviation of a normal distribution for each parameter.[1] A random value for each parameter is then extracted from the corresponding normal distribution using the 'super-wizz-o' algorithm described by Marsaglia & Zaman (1991) and implemented by Chandler & Northrop (2003), and 1000 random combinations of parameters are constructed. The combinations of parameters are normally distributed throughout the parameter ranges (Fig. 1). Being the geophysical model, a linear(ized) function of the parameters, the obtained predicted velocities are normally distributed too (Cramer 1957).

[1] The arithmetic mean between the maximum and the minimum values is assumed to be the mean of the normal distribution. The standard deviation is computed as the value leaving out of the minimum–maximum range a 1 per cent probability.

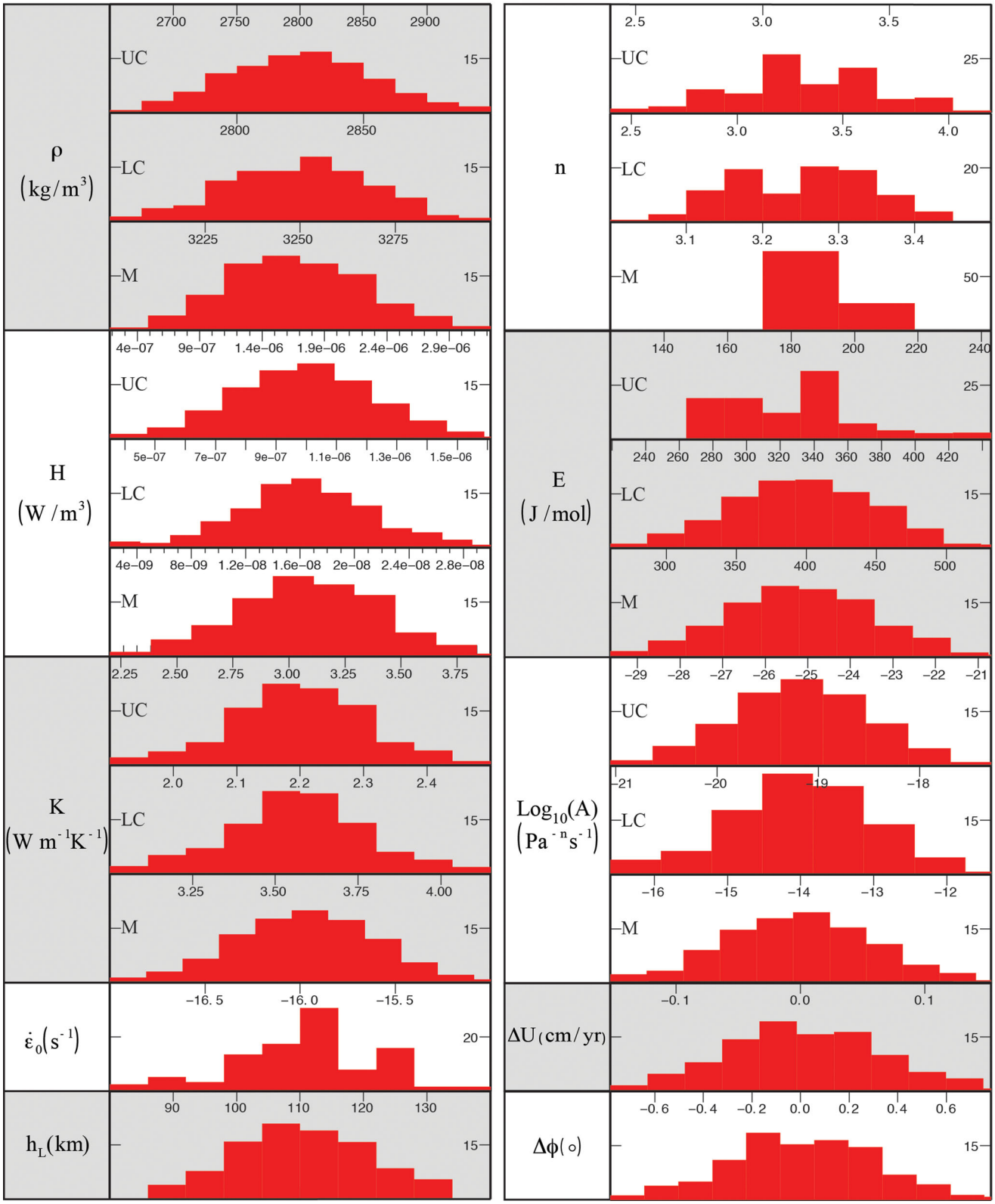


**Figure 1.** Distributions of the 1000 randomly extracted combinations of parameters

The 1000 combinations of parameters represent 1000 models that are used to predict the same number of velocity scenarios for the Mediterranean domain (Fig. 2). For each node $i$ of the numerical grid in the model (Fig. 3) and for each component of the horizontal velocity $V^i_{k,s}$, we compute

$$\bar{V}^i_k = \frac{1}{N_S}\sum_{s=1}^{N_S} V^i_{k,s} \quad (1)$$

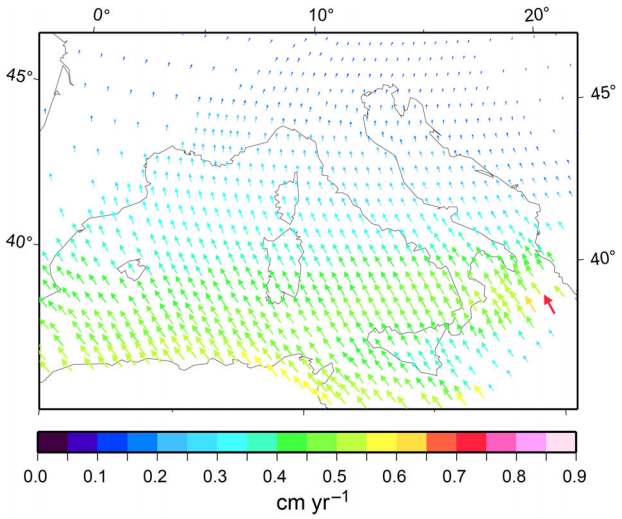


**Figure 2.** Example of predicted horizontal velocity scenario. Arrows represent the modelled velocity vectors at the nodes of the grid, with the corresponding intensity (colour map).

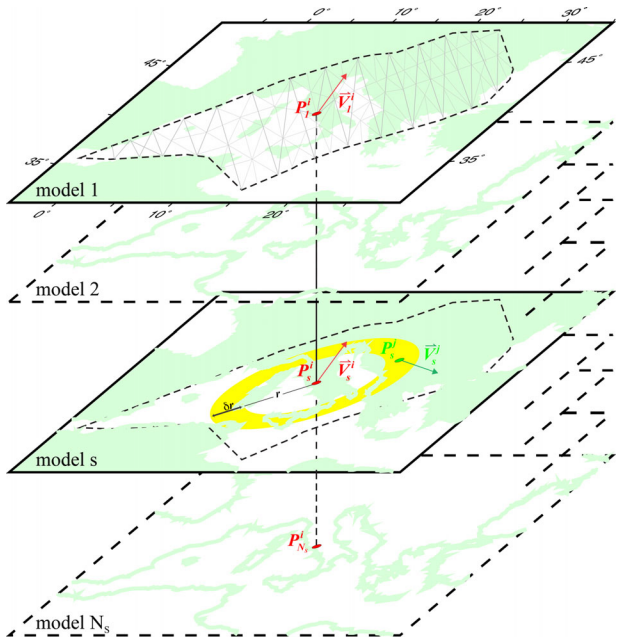


**Figure 3.** Scheme of the stable horizontal velocity scenarios used to evaluate the empirical covariance function. For each node $i$ of the grid, 30 circular rings (yellow colour) with a width $\delta r = 100$ km and an increasing radius $r$ are considered. The empirical covariance function is evaluated on the stack of the 79 stable velocity scenarios.

the 'mean velocity' of the $k$ component ($k = N, E$, where $N$ and $E$ stand for north and east) over the simulated velocity scenarios $N_S$ at node $i$ and

$$\delta V^i_{k,s} = V^i_{k,s} - \overline{V}^i_k \tag{2}$$

the 'residuals for the $k$ component with respect to the mean velocity' for node $i$ and scenario $s$.

The empirical autocovariance for each component $k$ of the model velocity is calculated as

$$C_{kk}\left(r_{ij}\right) = \frac{1}{N_s}\sum_{s=1}^{N_s}\left(\frac{1}{N}\sum_{i=1}^{N}\delta V^i_{k,s}\frac{1}{N_j}\sum_{j=1}^{N_j}\delta V^j_{k,s}\right)$$

$$= \frac{1}{N}\sum_{i=1}^{N}\left(\frac{1}{N}\sum_{s=1}^{N_s}\delta V^i_{k,s}\frac{1}{N_j}\sum_{j=1}^{N_j}\delta V^j_{k,s}\right), \tag{3}$$

where $k = N, E$, where $N$ and $E$ stand for north and east; node $i$ and node $j$ are distances such that $r_l < r_{ij} < r_l + \delta r$, $l = 0, 1, \ldots, N_l$, $r_0 = 0$; and $N_j$ is the number of nodes $j$ at a distance $r_{ij}$ from node $i$.

Similarly, the empirical cross-covariance between the two components $k$ and $k'$ is computed as

$$C_{kk'}\left(r_{ij}\right) = \frac{1}{N_s}\sum_{s=1}^{N_s}\left(\frac{1}{N}\sum_{i=1}^{N}\delta V^i_{k,s}\frac{1}{N_j}\sum_{j=1}^{N_j}\delta V^j_{k',s}\right)$$

$$= \frac{1}{N}\sum_{i=1}^{N}\left(\frac{1}{N}\sum_{s=1}^{N_s}\delta V^i_{k,s}\frac{1}{N_j}\sum_{j=1}^{N_j}\delta V^j_{k',s}\right). \tag{4}$$

A total of $N_l = 30$ circular rings with a width $\delta r = 100$ km is assumed for each node $i$, and the empirical auto- and cross-covariances of the model velocity components are estimated over the model area. These functions are shown in Fig. 4.

Although eq. (4) can be used to estimate the covariance function of a weak stationary and ergodic stochastic process, the estimated functions reproduce the signal structure of the modelled velocity field. The noise variance is negligible. In addition, the correlation lengths of the functions are related to the mean spacing between the grid nodes and the size of the model area (Barzaghi & Sansò 1983).

The calculations described in eqs (1)–(4) are performed after projecting the model grid onto a plane according to the Mercator projection of a spherical Earth (Grafarend & Krumm 2006)

$$x = R \cdot \cos\phi_0 \cdot (\vartheta - \vartheta_0)\,, \tag{5}$$

$$y = R \cdot \cos\phi_0 \cdot \ln\left[\mathrm{tg}\left(\frac{\pi}{4} + \frac{\phi}{2}\right)\right], \tag{6}$$

where $(\vartheta, \varphi)$ are the longitude and latitude and $(\vartheta_0, \varphi_0)$ are the chosen reference longitude and latitude. To minimize the deformation of the domain surface, we assumed $(\vartheta_0, \varphi_0) \equiv (13^\circ, 42^\circ)$, which are the mean longitude and latitude, respectively, of the investigated area.

The value at zero distance corresponds to the variance associated with the model-estimated velocities as implied by the uncertainties in the model parameters. The empirical auto- and cross-covariance trends also indicate that the model uncertainties are highly correlated at short to medium distances, that is, at a distance around 600 km. The empirical auto- and cross-covariances were then interpolated using a proper model covariance function allowing the positive definiteness of the associated covariance matrix. Of the many functions that can be used to interpolate the empirical covariances (Barzaghi & Sansò 1983), the function that best fits the empirical values shown in Fig. 4 is

$$C\left(r\right) = \frac{C_0}{1 + \left(\frac{r}{d}\right)^2}, \tag{7}$$

where $C_0$ and $d$ are selected to minimize the misfit between the empirical auto- and cross-covariances and the function (7).

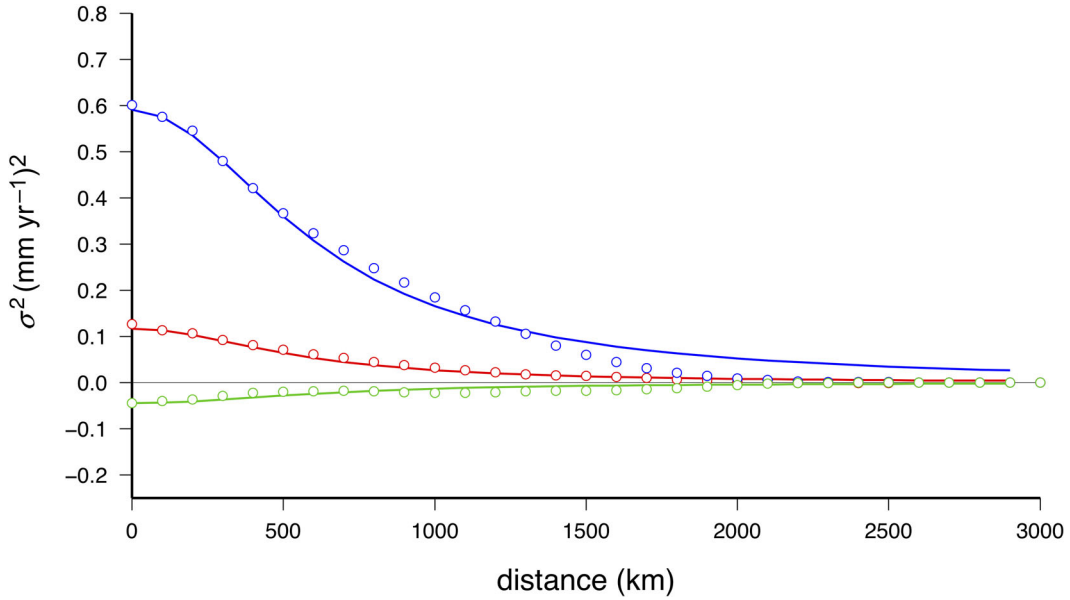


**Figure 4.** Comparison between the empirical (empty circles) and the model (continuum lines) covariance, as function of the distance, for the east component (red), the north component (blue) of the velocities and their cross-covariance (green). Empirical covariance is calculated by using eqs (3) and (4), assuming for each node $i$ $N_l = 30$ circular rings with a width $\delta r = 100$ km. The assumed model covariance function is described by the positive definite function of eq. (8), with the parameters selected in order to maximize the fit with the empirical covariance.

Comparisons between the empirical (empty circles) and model (solid lines) covariances for the east component $C_{EE}(r)$ (red) and the north component $C_{NN}(r)$ (blue) of the velocities and for their cross-covariance $C_{EN}(r)$ (green) are shown in Fig. 4. The model autocovariances are, by definition, positive definite. Furthermore, the spectra of the model auto- and cross-covariances satisfy the condition

$$|S_{EN}(s)|^2 \leq S_{EE}(s) \cdot S_{NN}(s). \tag{8}$$

This is a necessary and sufficient condition to be satisfied by the auto- and cross-covariance spectra of a bidimensional stochastic process.

Once this covariance structure has been estimated, uncertainties are assigned to the geophysical model's estimated velocities, which are then compared with the GPS-derived velocities using a $\chi^2$ analysis.

## COMPARATIVE STATISTICAL ANALYSIS

In this section, we show the results of a comparative analysis between the velocities predicted by the geophysical model (Fig. 5) and the GPS-derived velocities using a $\chi^2$ statistic.

If we consider an $n$-dimensional normal random variable $x$, with mean $\mu$ and covariance matrix $C$,

$$x = N(\mu, C), \tag{9}$$

it holds that being $C$ a symmetric positive definite matrix, it exists a symmetric positive definite matrix $K$ such that (Strang 1993)

$$C = K^2. \tag{10}$$

It then follows that

$$z = K^{-1}(x - \mu) \tag{11}$$

is a normal standard random variable. Hence, by definition

$$\chi_n^2 = z^t z = (x - \mu)^t C^{-1}(x - \mu) \tag{12}$$

is an $n$ degrees of freedom chi-square random variable (Cramer 1957).

Assuming that GPS-derived velocities are normally distributed with covariance $C$ and mean given by the model predicted velocities, we have then that

$$\chi^2 = R^T C^{-1} R, \tag{13}$$

where $R$ is defined as the difference between the data-derived velocities and the geophysical model predictions.

In the standard $\chi^2$ computation, the covariance matrix $C$ coincides with the diagonal, positive-definite covariance matrix of the GPS data only; thus, $C_{\text{data}}$ disregards the model uncertainty.

$$\chi^2_{\text{standard}} = R^T (C_{\text{data}})^{-1} R. \tag{14}$$

To account for the uncertainty in the predictive geophysical model, the proper matrix should be

$$C = C_{\text{data}} + C_{\text{model}}, \tag{15}$$

where $C_{\text{model}}$ represents the covariance matrix associated with the geophysical model and is calculated as specified in the previous section.

Thus, when the geophysical model covariance matrix is considered, the $\chi^2$ statistic can be expressed in the form

$$\chi^2_{\text{new}} = R^T (C_{\text{data}} + C_{\text{model}})^{-1} R, \tag{16}$$

where we now assume that the GPS and the model velocities have the same mean and are normal independent random variables with covariance matrices $C_{\text{data}}$ and $C_{\text{model}}$, respectively.

These hypotheses are fulfilled when model covariance is estimated according to the method described in the previous section. Thus eq. (14) can be evaluated versus eq. (16) in the framework of a standard $\chi^2$ test procedure (Cramer 1957).

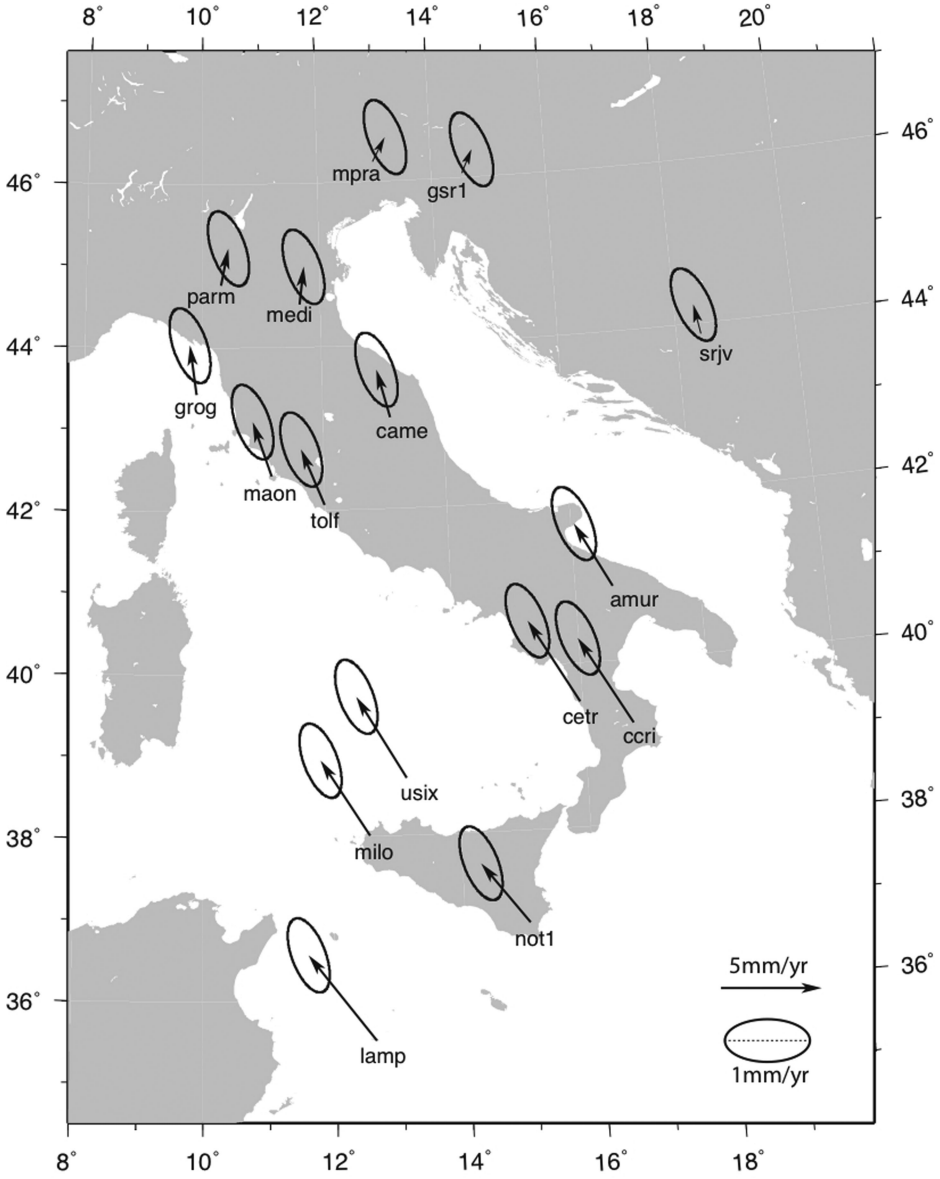


**Figure 5.** Example of modelled horizontal velocities with their uncertainties in terms of $3\sigma$ confidence ellipse.

### Velocity estimates from the observed GPS data

GPS-derived velocities, which are estimated at permanent stations distributed over the Earth's surface, are used in this type of predictive model. High-precision estimates of the station velocities can be obtained by modelling the daily time-series of the permanent GPS station coordinates. To perform the $\chi^2$ analysis, the set of permanent GPS stations and the corresponding residual vector $R$ and geophysical model covariance matrix $C_{\text{model}}$ must be specified. We use a GPS database composed of 54 stations that are distributed throughout the Italian Peninsula. The absolute velocities in the ITRF2005 (Altamimi *et al.* 2007) reference frame and the relative standard deviations are known for each station. To make the GPS-derived velocities compatible with the modelled velocities, we subtract the rigid motion of the Eurasia Plate, as calculated by Splendore *et al.* (2010), from the absolute GPS velocities before performing the $\chi^2$ analysis. Fig. 6 shows the obtained net GPS velocities, also listed in Table 2.

The residual vector $R$ represents the differences between the GPS-derived and model predictions. We interpolated the modelled nodal velocities at points coincident with the chosen permanent GPS stations using the same shape functions that were used to obtain the numerical solution. The geophysical model covariance matrix, $C_{\text{model}}$, is a symmetric square matrix; each cell contains the value of the model auto- and cross-covariance functions represented in Fig. 4 evaluated for the distances between the specific station pairs (Fig. 7).

### Predictive model

We used the same model used to build the model covariance matrix, assuming for the parameters values the means of the normal distributions shown in Table 1.

The predicted velocity scenario shows common large-scale features that agree with previous analyses (Marotta *et al.* 2004;

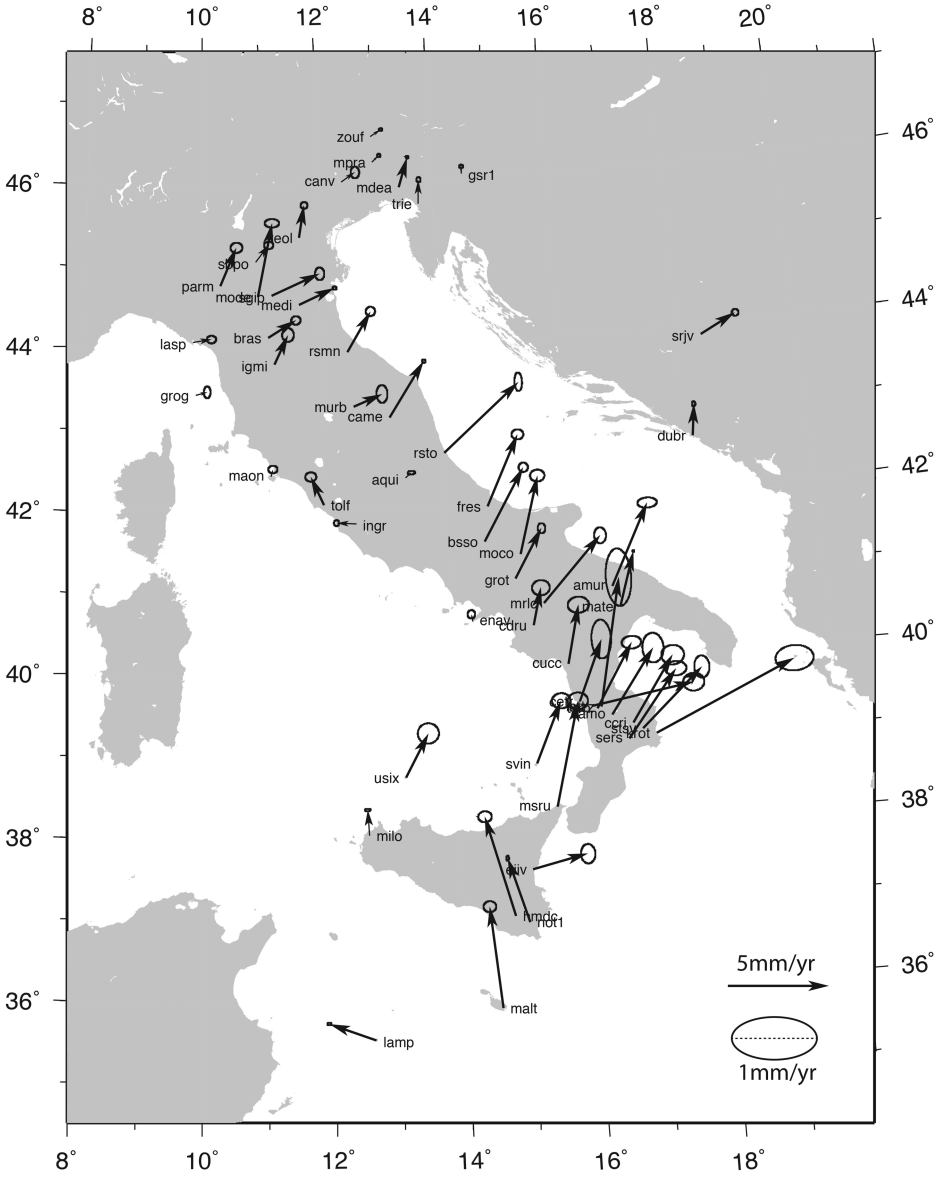


**Figure 6.** Net geodetic horizontal velocities (black arrows), obtained by subtracting the rigid motion of the Eurasia Plate, as calculated by Splendore et al. (2010), from the absolute GPS velocities, with their uncertainties in terms of the $3\sigma$ confidence ellipses at the permanent GPS stations considered for the comparative analysis. Absolute velocity solutions have been obtained by analysing the daily position solutions in the ITRF2005 reference frame.

Marotta & Sabadini 2008; Splendore *et al.* 2010), including dominantly northeastward-oriented velocities that rotate to the northwest across the model from south to north. Furthermore, the velocities tend to decrease with increasing distance from the Africa–Eurasia plate boundary (see Fig. 2).

The model predicted and GPS-derived velocities are then compared at the 54 GPS station locations using the standard formula (14) and the new devised formula (16). The two obtained values are, when divided for the degree of freedom (dof)

$$\chi^{2*}_{\text{standard}} = \frac{\chi^2_{\text{standard}}}{dof} = 705.53, \tag{17}$$

$$\chi^{2*}_{\text{new}} = \frac{\chi^2_{\text{new}}}{dof} = 37.72. \tag{18}$$

A sharp decrease in the sampled $\chi^2_{\text{new}}$ values is obtained with respect to $\chi^2_{\text{standard}}$ and this is expected due to the correct covariance matrix used in computing it.

## DISCUSSION AND CONCLUSIONS

A methodology has been developed to construct a model covariance matrix that allows for a more appropriate comparison between velocities predicted by geophysical models and those estimated from observed GPS data. The procedure leads to a definition of the model uncertainty, which is evaluated by randomly varying the parameters that influence the model estimates within admissible limiting values coming from literature. The covariance matrix associated with the model-derived velocities was estimated using numerical simulations, thus describing the model uncertainty in space. This information can be considered when performing the $\chi^2$ analysis to compare the geophysical model predictions with the GPS-derived estimated velocities.

Our case study demonstrates that beyond being more statistically appropriate, accounting for the model covariance matrix leads to a $\chi^{2*}$ value that has better statistical significance. In the application that has been described, the empirical $\chi^{2*}_{\text{new}}$ value drops down to

**Table 2.** List of the GPS-derived velocities with the corresponding standard deviations.

| Name | Lat. (deg) | Long. (deg) | $V_E$ (mm yr$^{-1}$) | $V_N$ (mm yr$^{-1}$) | $\sigma_E$ (mm yr$^{-1}$) | $\sigma_N$ (mm yr$^{-1}$) |
|---|---|---|---|---|---|---|
| aqui | 42.368 | 13.35 | 0.290112 | 0.251644 | 0.09 | 0.04 |
| amur | 40.907 | 16.604 | 2.0235 | 3.98492 | 0.23 | 0.12 |
| bras | 44.122 | 11.113 | 1.39264 | 0.850986 | 0.11 | 0.1 |
| bsso | 41.546 | 14.594 | 2.09774 | 3.57331 | 0.11 | 0.11 |
| came | 43.112 | 13.124 | 1.79224 | 2.73032 | 0.04 | 0.04 |
| camo | 39.34 | 16.449 | 2.25506 | 3.16795 | 0.25 | 0.35 |
| canv | 46.008 | 12.435 | 0.687437 | 0.466746 | 0.1 | 0.14 |
| ccri | 39.226 | 16.776 | 2.18043 | 3.20387 | 0.27 | 0.23 |
| cdru | 40.49 | 15.305 | 0.464209 | 1.84603 | 0.21 | 0.18 |
| cetr | 39.529 | 15.955 | 1.27183 | 3.01458 | 0.23 | 0.46 |
| cucc | 39.994 | 15.816 | 0.682345 | 2.89974 | 0.25 | 0.19 |
| dubr | 42.65 | 18.11 | 0.20609 | 1.5555 | 0.04 | 0.06 |
| eiiv | 37.514 | 15.082 | 2.7508 | 0.622974 | 0.17 | 0.23 |
| enav | 40.582 | 14.335 | −0.0515232 | 0.347382 | 0.09 | 0.1 |
| fres | 41.974 | 14.669 | 1.67253 | 3.48087 | 0.14 | 0.12 |
| grog | 43.426 | 9.892 | 0.559167 | 0.151393 | 0.08 | 0.14 |
| grot | 41.073 | 15.06 | 1.42116 | 2.42071 | 0.09 | 0.12 |
| gsr1 | 46.048 | 14.544 | −0.00663473 | 0.36827 | 0.05 | 0.04 |
| hmdc | 36.959 | 14.783 | −1.29794 | 4.99241 | 0.16 | 0.13 |
| igmi | 43.796 | 11.214 | 0.698232 | 1.45955 | 0.14 | 0.16 |
| ingr | 41.828 | 12.515 | −0.975904 | 0.0740094 | 0.06 | 0.07 |
| krot | 39.08 | 17.125 | 7.09696 | 3.14278 | 0.45 | 0.3 |
| lamp | 35.5 | 12.606 | −2.30622 | 0.882304 | 0.05 | 0.03 |
| lasp | 44.073 | 9.84 | 0.920816 | 0.147311 | 0.11 | 0.09 |
| latt | 39.463 | 16.138 | 5.12916 | 0.834202 | 0.25 | 0.21 |
| luzz | 39.446 | 16.288 | 1.30111 | 6.35042 | 0.3 | 0.68 |
| malt | 35.838 | 14.526 | −0.447026 | 5.06646 | 0.15 | 0.13 |
| maon | 42.428 | 11.131 | 0.104004 | 0.352497 | 0.11 | 0.09 |
| mate | 40.649 | 16.704 | 0.856959 | 2.69592 | 0.02 | 0.02 |
| mdea | 45.924 | 13.436 | 0.475371 | 1.45982 | 0.03 | 0.03 |
| medi | 44.52 | 11.647 | 1.785 | 0.796751 | 0.05 | 0.04 |
| milo | 38.008 | 12.584 | −0.0537554 | 1.2803 | 0.07 | 0.03 |
| moco | 41.371 | 15.159 | 1.06368 | 3.83091 | 0.17 | 0.14 |
| mode | 44.629 | 10.949 | 0.742576 | 3.6372 | 0.17 | 0.1 |
| mpra | 46.241 | 12.988 | 0.33687 | 0.317574 | 0.04 | 0.04 |
| mrlc | 40.756 | 15.489 | 2.98469 | 3.16524 | 0.14 | 0.19 |
| msru | 38.264 | 15.508 | 1.31475 | 5.16724 | 0.24 | 0.2 |
| murb | 43.263 | 12.525 | 1.43505 | 0.574921 | 0.13 | 0.21 |
| not1 | 36.876 | 14.99 | −0.944924 | 3.21352 | 0.03 | 0.06 |
| parm | 44.765 | 10.312 | 0.796091 | 1.88486 | 0.14 | 0.12 |
| rsmn | 43.933 | 12.451 | 1.19936 | 1.96818 | 0.11 | 0.11 |
| rsto | 42.658 | 14.001 | 3.83526 | 3.31443 | 0.09 | 0.22 |
| sbpo | 45.051 | 10.92 | 0.64853 | 0.834776 | 0.11 | 0.09 |
| sers | 39.036 | 16.689 | 2.56044 | 3.29426 | 0.25 | 0.17 |
| sgip | 44.636 | 11.183 | 2.39988 | 1.0569 | 0.11 | 0.15 |
| srjv | 43.868 | 18.414 | 1.80032 | 0.891178 | 0.08 | 0.08 |
| stsv | 39.148 | 16.915 | 3.14353 | 2.81931 | 0.18 | 0.26 |
| svin | 38.803 | 15.234 | 1.35717 | 3.03867 | 0.22 | 0.18 |
| teol | 45.343 | 11.677 | 0.273627 | 1.59937 | 0.08 | 0.08 |
| tolf | 42.064 | 12 | −0.632943 | 1.42775 | 0.13 | 0.11 |
| trie | 45.71 | 13.764 | 0.062538 | 1.19133 | 0.05 | 0.06 |
| tvrn | 39.431 | 16.226 | 1.90867 | 3.14372 | 0.23 | 0.15 |
| usix | 38.708 | 13.179 | 1.17989 | 2.13547 | 0.25 | 0.24 |
| zouf | 46.557 | 12.974 | 0.515747 | 0.316285 | 0.04 | 0.03 |

37.72, contrary to the empirical $\chi^{2*}_{\text{standard}}$ value that is almost two orders of magnitude higher.

As a final remark, we underline that this methodology can be applied to any physical model for which a set of parameters significantly influences the variability of the results. For instance, similar methodologies are used in meteorological and oceanographic data assimilation procedures (Lorenc 2011).

## ACKNOWLEDGEMENTS

The authors thank the Editor, the reviewers Carl Christian Tscherning and three anonymous for the constructive criticisms. All figures have been created by GMT plotting software (Wessel & Smith 2001).

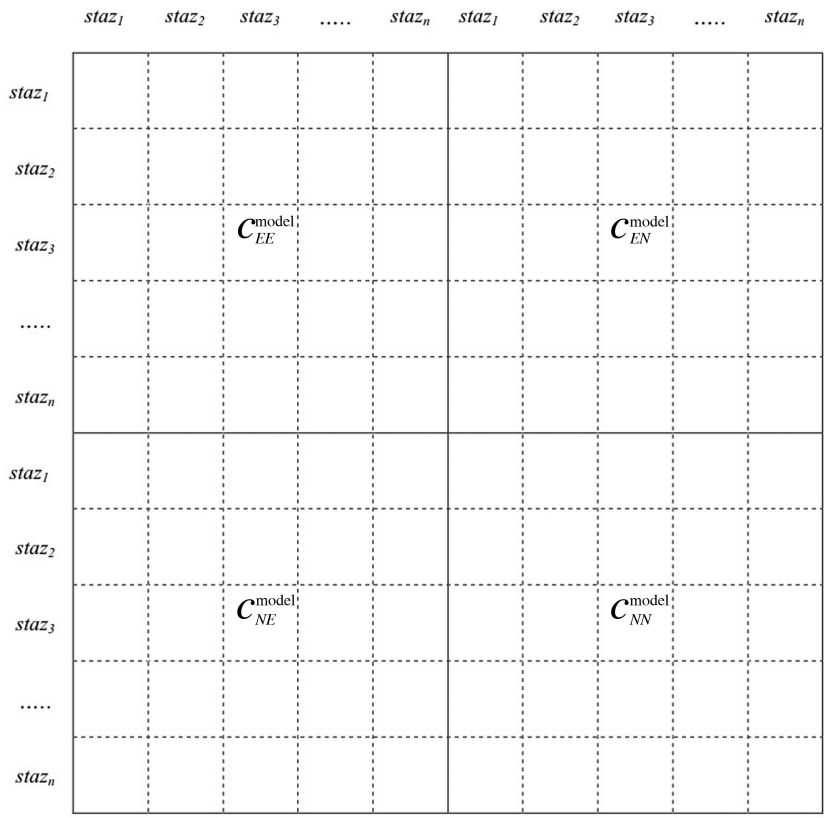


**Figure 7.** Scheme of the model covariance matrix $C_{\text{model}}$. $C_{\text{model}}$ is a symmetric square matrix, with each cell containing the value of the model auto- ($C_{EE}$ and $C_{NN}$) and cross- ($C_{EN}$ and $C_{NE}$) covariance functions evaluated for the mutual distances between the specific considered couple of stations ($staz_1$ to $staz_n$).

## REFERENCES


Afonso, J.C. & Ranalli, G., 2004. Crustal and mantle strengths in continental lithosphere: is the jelly sandwich model obsolete? *Tectonophysics,* **394,** 221–232.

Altamimi, Z., Collilieux, X., Legrand, J., Garayt, B. & Boucher, C., 2007. ITRF2005: a new release of the International Terrestrial Reference Frame based on time series of station positions and Earth Orientation Parameters, *J. geophys. Res.,* **112,** B09401, doi:10.1029/2007JB004949.

Artemieva, I. & Mooney, W.D., 2001. Thermal thickness and evolution of Precambrian lithosphere: a global study, *J. geophys. Res.,* **106**(B8), 16 387–16 414.

Barker, C., 1996. *Thermal Modeling of Petroleum Generation: Theory and Applications,* Elsevier.

Barzaghi, R. & Sansò, F., 1983. Sulla stima empirica della funzione di covarianza, *Boll. Geod. Sci. Aff.,* **4,** 389–415.

Beardsmore, G.R. & Cull, J.P., 2001. *Crustal Heat Flow: A Guide to Measurement and Modelling,* Cambridge Univ. Press.

Chandler, R. & Northrop, P., 2003. Randgen.f., Available at: http://www.ucl.ac.uk/~ucakarc/work/randgen.html (last accessed March 2012).

Chopra, P.N. & Peterson, M.S., 1981. The experimental deformation of dunite, *Tectonophysics,* **78,** 453–473.

Cramer, H., 1957. *Mathematical Methods of Statistics,* Princeton Univ. Press.

Drury, M.J., 1986. Thermal conductivity, thermal diffusivity, density and porosity of crystalline rocks, *Technical Report, 86-5,* Earth Physics Branch, Ottawa.

Grafarend, E.W. & Krumm, F.W., 2006. *Map Projections: Cartographic Information System,* Springer.

Hansen, F. & Carter, N., 1982. Creep of selected crustal rocks at 1000 MPa, *EOS, Trans. Am. geophys. Un.,* **63,** 437.

Jiménez-Munt, I., Sabadini, R., Gardi, A. & Bianco, G., 2003. Active deformation in the Mediterranean from Gibraltar to Anatolia inferred from numerical modelling, geodetic and seismological data, *J. geophys. Res.,* **108**(B1), doi:10.1029/2001JB001544.

Lorenc, A.C., 2011. Developments of variational data assimilation, in *Proceedings of ECMWF Seminar on Data Assimilation for Atmosphere and Ocean,* 6–9 Sep.

Marotta, A.M. & Sabadini, R., 2004. The signatures of tectonics and glacial isostatic adjustment revealed by the strain rate in Europe, *Geophys. J. Int.,* **157,** 865–870.

Marotta, A.M. & Sabadini, R., 2008. Africa–Eurasia kinematics control of long-wavelength tectonic deformation in the central Mediterranean, *Geophys. J. Int.,* **175,** 742–754.

Marotta, A.M., Mitrovica, J.X., Sabadini, R. & Milne, G., 2004. Combined effects of tectonics and glacial isostatic adjustment on intraplate deformation in central and northern Europe: applications to geodetic baseline analyses, *J. geophys. Res.,* **109,** doi:10.1029/2002JB002337.

Marsaglia, G. & Zaman, A., 1991. A new class of random number generators, *Ann. Appl. Probab.,* **1**(3), 462–480.

Ranalli, G. & Murphy, D.C., 1987. Rheological stratification of the lithosphere, *Tectonophysics,* **132,** 281–295.

Ray, L., Kumar, P.S., Reddy, S.R.G.K., Rao, G.V., Srinivasan, R. & Rao, R.U.M., 2003. High mantle heat flow in a Precambrian granulite province: evidence from southern India, *J. geophys. Res.,* **108**(B2), doi:10.1029/2001JB000688.

Roy, R.F., Beck, A.E. & Touloukian, Y.S., 1981. Thermophysical properties of rocks, in *Physical Properties of Rocks and Minerals,* eds Touloukian, Y.S., Judd, W.R. & Roy, R.F., McGraw-Hill.

Rybach, L., 1988. Determination of heat production rate, in *Handbook of Terrestrial Heat Flow Density Determination,* eds Haenel, R., Rybach, L. & Stegena, L., Kluwer.

Schaocheng, J., Pinglao, Z. & Bin, X., 2003. Flow laws of multiphase materials and rocks from end-member flow laws, *Tectonophysics,* **370,** 129–145.

Splendore, R., Marotta, A.M., Barzaghi, R., Borghi, A. & Cannizzaro, L., 2010. Block model versus thermo-mechanical model: new insights on the

present-day regional deformation in the surroundings of the Calabrian Arc, in *Advances in Interpretation of Geological Processes: Refinement of Multi-Scale Data and Integration in Numerical Modelling,* Vol. **332,** pp. 129–147, eds Spalla, M.I., Marotta, A.M. & Gosso, G., Geological Society, Special Publications.

Strang, G., 1993. *Introduction to Linear Algebra,* Wellesley-Cambridge Press.

Tesauro, M., Kabal, M.K. & Cloetingh, S.P.L., 2008. EuCRUST-07: a new reference model for the European crust, *Geophys. Res. Lett.,* **35,** L05313, doi:10.1029/2007GL032244.

Vilà, M., Fernández, M. & Jiménez-Munt, I., 2010. Radiogenic heat production variability of some common lithological groups and its significance to lithospheric thermal modeling, *Tectonophysics,* **490,** 152–264.

Weertman, J. & Weertman, J.R., 1975. High temperature creep of rock and mantle viscosity, *Annu. Rev. Earth planet. Sci.,* **3,** 293–315.

Wessel, P. & Smith, W.M., 2001. New improved version of generic mapping tools released, *EOS, Trans. Am. geophys. Un.,* **79,** 579.

## APPENDIX: NUMERICAL MODEL SETTINGS

The physics of the crust–mantle system during tectonic convergence is described by the vertically integrated momentum equation

$$\frac{\partial}{\partial\vartheta}\left[2\bar{\mu}\left(\frac{\partial}{\partial\vartheta}u_\vartheta + u_\mathrm{r}\right)\right] + \frac{1}{\sin\vartheta}\frac{\partial}{\partial\varphi}\left[\bar{\mu}\left(\frac{1}{\sin\vartheta}\frac{\partial}{\partial\varphi}u_\vartheta + \frac{\partial}{\partial\vartheta}u_\varphi - u_\varphi\cot\vartheta\right)\right] + \left[2\bar{\mu}\left(\frac{\partial}{\partial\vartheta}u_\vartheta - \frac{1}{\sin\vartheta}\frac{\partial}{\partial\varphi}u_\varphi - u_\vartheta\cot\vartheta\right)\right]\cot\vartheta$$
$$= \frac{g\rho_\mathrm{c}R}{2H_\mathrm{L}}\left(1-\frac{\rho_\mathrm{c}}{\rho_\mathrm{m}}\right)\frac{\partial}{\partial\vartheta}S^2,$$

$$\frac{\partial}{\partial\vartheta}\left[\bar{\mu}\left(\frac{1}{\sin\vartheta}\frac{\partial}{\partial\varphi}u_\vartheta + \frac{\partial}{\partial\vartheta}u_\varphi - u_\varphi\cot\vartheta\right)\right] + \frac{1}{\sin\vartheta}\frac{\partial}{\partial\varphi}\left[2\bar{\mu}\left(\frac{1}{\sin\vartheta}\frac{\partial}{\partial\varphi}u_\vartheta + \frac{\partial}{\partial\vartheta}u_\varphi - u_\varphi\cot\vartheta\right)\right]\cot\vartheta = \frac{g\rho_\mathrm{c}R}{2H_\mathrm{L}}\left(1-\frac{\rho_\mathrm{c}}{\rho_\mathrm{m}}\right)\frac{1}{\sin\vartheta}\frac{\partial}{\partial\varphi}S^2 \tag{A1}$$

numerically solved within a spherical 2-D domain. $u_\vartheta$, $u_\varphi$ and $u_\mathrm{r}$ are the velocity components along the colatitudes, longitude and the radius, respectively, $\vartheta$ is the colatitude, $\varphi$ is the longitude, $S$ is the crustal thickness, $H_\mathrm{L}$ is the lithosphere thickness, $\rho_\mathrm{c}$ and $\rho_\mathrm{m}$ are the density of the

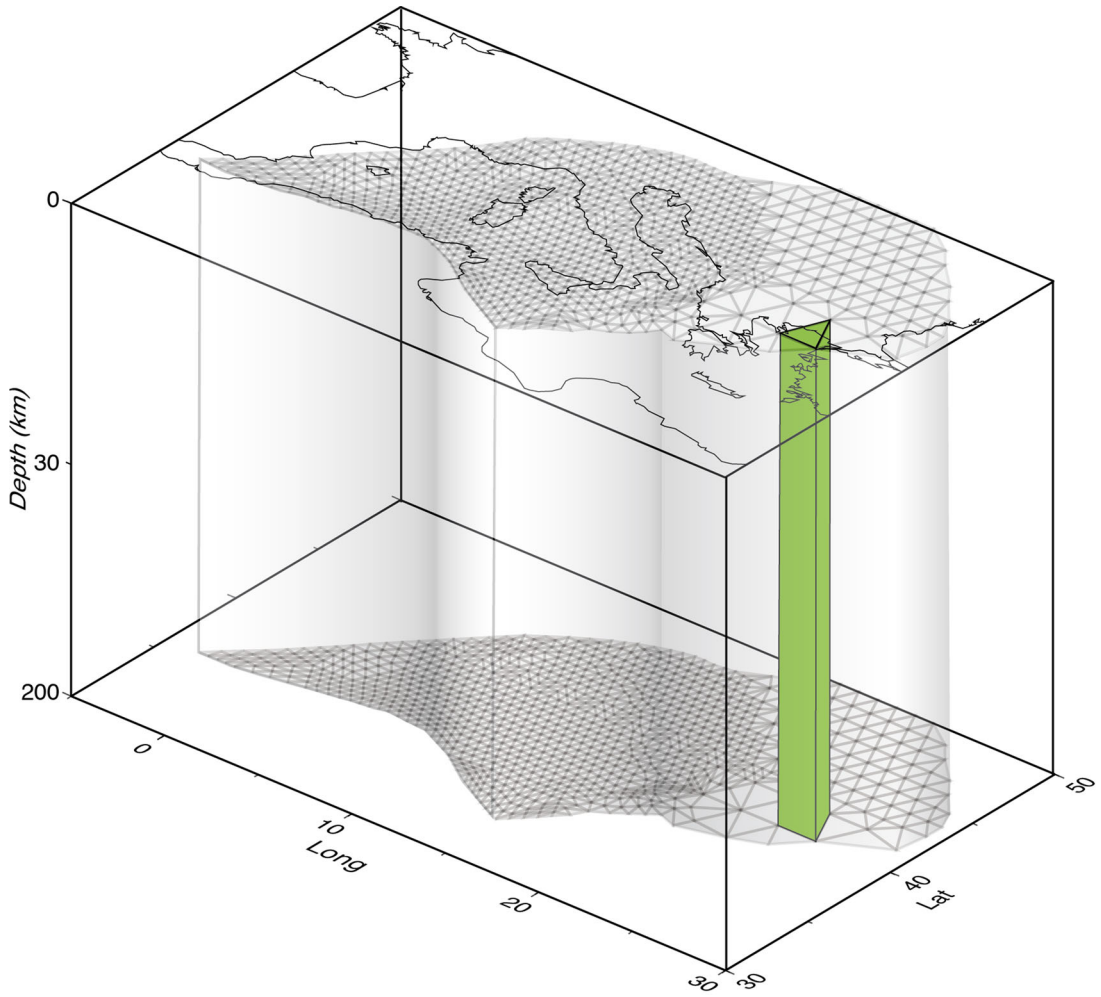


**Figure A1.** 3-D scheme used for the thermomechanical model.

crust and the mantle, respectively, $g$ is the gravity acceleration and $R$ is the terrestrial radius. The used crustal thickness is obtained by linear interpolation onto the adopted numerical grid of model EuCRUST-07 (Tesauro *et al.* 2008).

$\bar{\mu}$ is the vertically averaged viscosity of the lithosphere, based on lithosphere thermal state and rheological parameters assumed for crust and mantle. It is calculated as

$$\bar{\mu} = \frac{1}{\dot{\varepsilon}} \int_0^{H_L} \sigma_y \mathrm{d}y, \tag{A2}$$

where $\sigma_y$ is lithosphere strength, calculated by assuming that rocks behave like a brittle or a ductile material according to their composition and thermal state.

For the brittle behaviour, a linear failure criterion is assumed in the form (Ranalli & Murphy 1987)

$$\sigma_B = (\sigma_H - \sigma_V)_B = \beta\, r\, \rho\, g, \tag{A3}$$

where $r$ is the depth along the terrestrial radius, $\rho$ is the density, $g$ is the acceleration of gravity and $\beta$ a parameter depending on the type of faulting and assumed equal to 3 for thrust faulting, 1.2 for strike slip faulting and 0.75 for normal faulting (Ranalli & Murphy 1987).

For the ductile behaviour, the power law is assumed in the form (Weertman & Weertman 1975)

$$\sigma_D = (\sigma_H - \sigma_V)_D = \left(\frac{\dot{\varepsilon}}{\dot{\varepsilon}_0}\right)^{\frac{1}{n}} \cdot \exp\left(\frac{E_a}{nRT}\right), \tag{A4}$$

where $\dot{\varepsilon}$ is the strain rate, ranged between $10^{-19}$ and $10^{-16}$ $\mathrm{s}^{-1}$; $R$ is the universal constant of gas, $\dot{\varepsilon}_0$, $n$ and $E_\mathrm{a}$ constant characteristics of the rocks.

$T$ is the 3-D lithosphere temperature and is determined by solving the steady-state energy equation in the form

$$\nabla \cdot (K\, \nabla T) + \rho H = 0 \tag{A5}$$

on a 3-D grid (Fig. A1), composed by prismatic elements obtained by projecting along the depth the 2-D numerical grid used in the tectonic model. $K$ is the thermal conductivity, $\rho$ is the density and $H$ the rate of radiogenic heat production per unit mass.